Journal of Structural Chemistry. Vol. 58, No. 7, pp. 1332-1340, 2017.

MOLECULAR STRUCTURES, HIRSHFELD SURFACE ANALYSIS, AND SPECTROSCOPIC PROPERTIES OF 6,8-DIMETHYL-3-(4-CHLOROPHENYL)-7-OXO-7,8-DIHYDROPYRIMIDO[4,5-*c*]PYRIDAZIN-5(6*H*)-ONE AND 6,8-DIMETHYL-3-(4-CHLOROPHENYL)-7-THIOXO-7,8-DIHYDROPYRIMIDO[4,5-*c*]PYRIDAZIN-5(6*H*)-ONE

A. Poursattar Marjani[1], M. R. Taghartapeh[2], A. R. Soltani[2,3]*, J. Khalafy[1], and Y. Kanani[3]

UDC 541.6:547.021

X-ray crystallography images are used to perform DFT studies of the structural, electronic, intermolecular energies and IR frequencies of 6,8-dimethyl-3-(4-chlorophenyl)-7-oxo-7,8-dihydropyrimido[4,5-*c*]pyridazin-5(6*H*)-one (**A**) and 6,8-dimethyl-3-(4-chlorophenyl)-7-thioxo-7,8-dihydropyrimido[4,5-*c*]pyridazin-5(6*H*)-one (**B**) using Gaussian 98 and Crystal Explorer program packages. The optimization of **A** and **B** in vacuum and solvent (ethanol) phases represent negligible changes in the bond distances, bond angles, and torsion angles. Moreover, the optimization in ethanol is closer to the X-ray crystallography data as compared to the gas phase. Moreover, the Hirshfeld surface analysis reveals that the highest amount of close contact contributions relates to H---H contacts while the lowest amount goes to Cl---Cl/Cl---Cl and C---O/O---C close contacts for **A** and **B**, respectively. The corresponding calculated IR intensity values highly match the experimental data.

DOI: 10.1134/S0022476617070095

Keywords: X-ray crystallography, DFT, electronic properties, hirshfeld surface analysis.

INTRODUCTION

Pyridazine derivatives are the important class of heterocyclic compounds due to their biological and pharmaceuitical applications, such as analgesics, bactericides, cardiotonics, fungicides, and insecticides [1-8]. In the chemical literature three isomers of pyrimido[4,5-*c*]pyridazine, pyrimido[4,5-*d*]pyridazine and pyrimido[5,4-*c*]pyridazine have been reported for the pyrimidopyridazines. The monoamine oxidase (MAO) inhibitory activities of pyrimidopyridazines have been reported by

[1]Department of Chemistry, Faculty of Science, Urmia University, Urmia, Iran. [2]Young Researchers and Elite Club, Gorgan Branch, Islamic Azad University, Gorgan, Iran. [3]Golestan Rheumatology Research Center, Golestan University of Medical Science, Gorgan, Iran; alireza.soltani46@yahoo.com. The text was submitted by the authors in English. *Zhurnal Strukturnoi Khimii*, Vol. 58, No. 7, pp. 1371-1378, September-October, 2017. Original article submitted December 22, 2015; revised April 3, 2016.

Caroti and co-workers [9]. The pyrimidopyridazines are used as a potential therapeutic agent as well [10-12]. The comparisons of theoretical and experimental structures of chemical compounds have been a source of attention in recent years.

Moreover, a broad variety of theoretical investigations of the structural, electronic, and spectroscopic properties of organic and organometallic compounds in order to further compare and consider over the probable benefits of these compounds have been reported [13-18]. The previous reports on aminoethylphosphonic acid prepared by Roldan and novel quinonediimines reported by SeinJr are some among many reports published so far [13, 14].

To the best of our knowledge, there are few reports focusing on the DFT studies of pyrimidopyridazines. Hence, in the present work we performed a computational investigation of two pyrimidopyridazines (**A** and **B**) and compared the computational data with the experimental results where possible. Furthermore, the Hirshfeld surface analysis of **A** and **B** was computationally studied for the better understanding of intermolecular interactions in **A** and **B**.

EXPERIMENTAL

Synthesis. Pyrimidopyridazines (**A** and **B**) have been regioselectively synthesized via the one-pot three-component reaction of 1,3-dimethylbarbituric acid (**1a**) or 1,3-dimethylthiobarbituric acid (**1b**) with 4-chlorophenylglyoxal in the presence of hydrazinium dihydrochloride in ethanol [19].

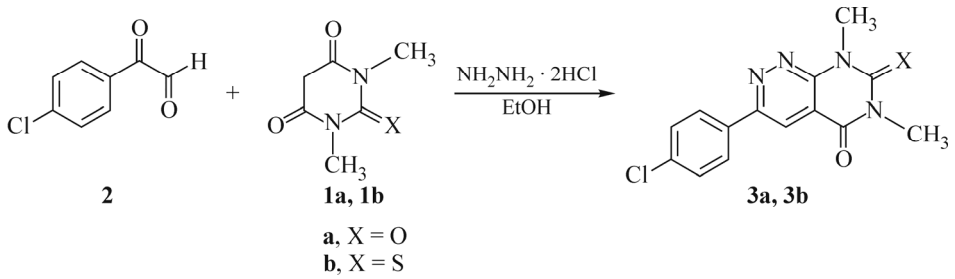

2 **1a, 1b** **3a, 3b**

a, X = O
b, X = S

Scheme 1. The synthesis of pyrimidopyridazines (**3a = A**) and (**3b = B**).

Crystal structure. Crystal data, data collection procedure, structure determination methods and refinement results for **A** and **B** are summarized in Table 1. The ORTEP drawing of the studied molecules (**A** and **B**) and the corresponding H bonds of **A** are shown in Fig. 1.

COMPUTATIONAL ANALYSIS

Computational details. At first, we have modeled **A** and **B** with the Chem Draw package. Then the energy minimization was performed using Chem 3D. The DFT molecular calculations were carried out using the Gaussian 98 quantum chemistry software [20]. We have calculated the geometric parameters of **A** and **B** in the ground state using Becke′s three-parameter hybrid method with the Lee *et al*. correlation functional methods (B3LYP) with the 6-311++G** basis set in gas and solvent (H_2O) phases [21, 22]. We also indicated the solvent effects using the integral equation formalism of the polarizable continuum model (PCM), and ethanol has been considered as a solvent. All the analyses of the structural and electronic properties were calculated using the Gaussview 3.0 package [23].

Vibrational frequencies for both structures have been calculated with the B3LYP functional and the 6-311++G** standard basis set. The HOMO-LUMO energy gap and relevant quantum molecular descriptors [24-27] are also calculated using the corresponding HOMO and LUMO values as below:

$$\mu = -(I + A)/2, \quad (1)$$

$$\eta = (I - A)/2, \quad (2)$$

TABLE 1. X-ray Crystallography and Calculation Results for **A** and **B**

Compound	**A = 3a**	**B = 3b**
Empirical formula	$C_{14}H_{11}ClN_4O_2$	$C_{14}H_{11}ClN_4OS$
Formula weight, g/mol^{-1}	302.72	318.78
Crystal size, mm	0.30×0.10×0.06	0.50×0.30×0.06
Crystal shape, colour	Plate, white	Plate, light yellow
Temperature, K	296(2)	296(2)
Wavelength, Å	0.71073	0.71073
Crystal system; Space group	Triclinic; *P*-1	Triclinic; *P*-1
a, *b*, *c*, Å	7.698(3), 8.023(3), 12.459(5)	7.8832(15), 8.0873(15), 12.907(2)
α, β, γ, deg.	80.335(5), 75.103(6), 62.229(5)	83.828(2), 73.461(2), 62.068(2)
V, Å^3; *Z*	657.0(4); 2	696.6(2); 2
Density, g/m^3	1.530	1.520
Absorption coefficient μ, mm^{-1}	0.301	0.427
Maximum and minimum transmission	0.9822 and 0.9151	0.9748 and 0.8147
θ range for data collection, deg.	1.69-28.34	2.85-28.27
Index ranges	$-10 \le h \le 10$, $-10 \le k \le 10$, $-16 \le l \le 16$	$-10 \le h \le 10$, $-10 \le k \le 10$, $-17 \le l \le 17$
Collected / Independent reflections (R_{int})	8085 / 3212 (0.0479)	8611 / 3296 (0.0247)
Refinement method	Full-matrix least-squares on F^2	
Goodness-of-fit on F^2	1.010	1.034
Final *R* indices [$I > 2\sigma(I)$]	$R_1 = 0.0741$, $wR_2 = 0.1816$	$R_1 = 0.0473$, $wR_2 = 0.1320$
R indices (all data)	$R_1 = 0.01334$, $wR_2 = 0.2164$	$R_1 = 0.0582$, $wR_2 = 0.1436$
Largest difference in peak and hole, e/Å^3	0.438 and –0.245	0.324 and –0.222

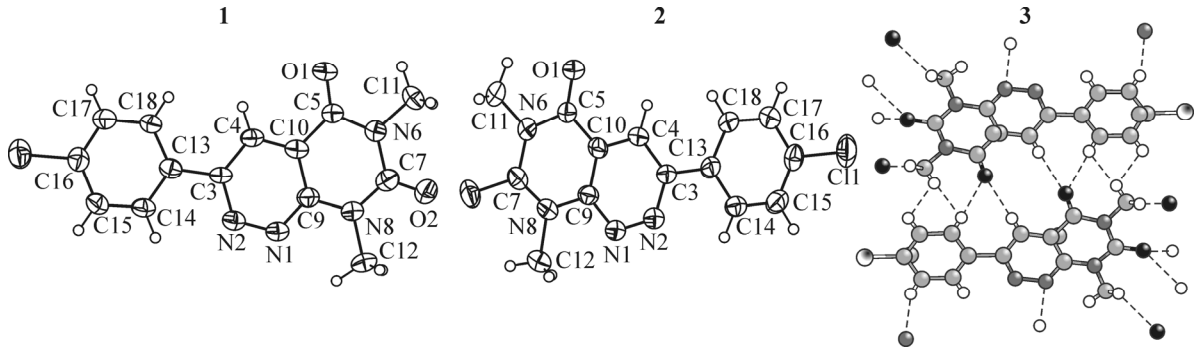

Fig. 1. Molecular single crystal plots of **1** = **A** and **2** = **B** and the crystal packing showing zigzag H bonds of **A** (**3**).

$$S = 1/2\eta, \quad (3)$$

$$\omega = (\mu^2/2\eta), \quad (4)$$

where I and A are the ionization potential and electron affinity of the system, respectively. E_{HOMO}: energies of the highest occupied molecular orbital plus the first eigenvalue of the valence band. E_{LUMO}: energies of the lowest unoccupied molecular orbital. Electronegativity χ is determined as the negative chemical potential μ as follows: $\chi = -\mu$. Chemical hardness η and softness *S* can be determined using the Koopmans theorem [28]. The electrophilicity index ω is calculated from the energy stabilization when the system obtains an additional electronic charge Δ*N* from the environment, as defined by Parr *et al*. [29].

Geometry optimization. In this paper, all the geometry optimizations and structural simulations of two **A** and **B** compounds were theoretically studied using the Gaussian 98 quantum chemistry software with the B3LYP method and 6-311++G** basis sets in both gas and solvent phases. As it is clear from Table 2, there are negligible changes in the binding

TABLE 2. Some Experimental and Calculated Bond Lengths for **A** and **B** in the Gas and Solvent Phases

Bond lengths	**A**			Bond lengths	**B**		
	Exp.	Gas	Solvent		Exp.	Gas	Solvent
N1–C9	1.32(4)	1.34	1.34	N1–C9	1.32(4)	1.34	1.34
N1–N2	1.33(4)	1.32	1.32	N1–N2	1.33(4)	1.32	1.32
N2–C3	1.35(4)	1.35	1.34	N2–C3	1.34	1.38	1.35
C3–C4	1.40(4)	1.40	1.40	C3–C4	1.40	1.40	1.40
C3–C13	1.48(4)	1.48	1.48	C3–C13	1.48	1.48	1.48
C4–C10	1.36(4)	1.38	1.38	C4–C10	1.37	1.38	1.38
C4–H4	0.93	1.08	1.08	C4–H4	0.93	1.08	1.08
C5–O1	1.21(4)	1.22	1.22	C7–S1	1.65	1.67	1.68
C5–N6	1.38(4)	1.39	1.39	C5–N6	1.39	1.40	1.40
C5–C10	1.47(4)	1.48	1.47	C5–C10	1.46	1.47	1.47
N6–C7	1.41(4)	1.41	1.41	N6–C7	1.40	1.47	1.40
N6–C11	1.46(4)	1.47	1.47	C7–N8	1.37	1.38	1.38
C7–O2	1.21(4)	1.21	1.22	N8–C9	1.38	1.39	1.39
C7–N8	1.37(4)	1.39	1.39	N8–C12	1.48	1.48	1.48
N8–C9	1.37(4)	1.38	1.38	C9–C10	1.40	1.40	1.40
N8–C12	1.47(4)	1.47	1.47	C11–H11	0.96	1.09	1.08
C9–C10	1.40(4)	1.40	1.40	C12–H12	0.96	1.08	1.08
C11–H11	0.96	1.08	1.08	C16–C17	1.38	1.39	1.39
C12–H12	0.96	1.08	1.08	C17–C18	1.38	1.39	1.39
C16–C17	1.37(5)	1.39	1.39	C16–Cl1	1.74	1.76	1.76
C17–C18	1.38(5)	1.39	1.39				
C16–Cl1	1.74(3)	1.76	1.76				

distances calculated in the gas phase as compared with the experimental crystallography data for **A**. The binding distances between N1–N2, N8–C9, C7–O2, N6–C5, C5–O1, C3–C13, and C16–C11 of 1.33 Å, 1.37 Å, 1.21 Å, 1.38 Å, 1.21 Å, 1.48 Å, and 1.74 Å (experimental data) changed to 1.32 Å, 1.38 Å, 1.21 Å, 1.39 Å, 1.22 Å, 1.48 Å, and 1.76 Å (calculated data for the gas phase), respectively, which show minor changes from the binding distances obtained from the crystallography data. For the further understanding and comparison of the solvent effect on the binding distances in **A**, and since we predict less differences in the binding distances for **A**, we optimized it in ethanol as a solvent.

As it is clear from Table 2, in comparison with the experimental crystallography data, the differences in the binding distances for the geometry optimization in ethanol were less than those in the vacuum). Using ethanol for the optimization, the bond distance for N1–N2, N8–C9, C5–N6, C5–O1, and C3–C13 represented the values of 1.32 Å, 1.38 Å, 1.39 Å, 1.22 Å, and 1.48 Å, and it is very close to the experimental data for C7–O2 and C16–Cl1 bonds of 1.22 Å and 1.39 Å, respectively, and interestingly, also for C3–C13 and N6–C7 bonds having the values of 1.48 Å and 1.41 Å in both experimental [19] and computational data. These results account for the greater reliability of the extracted data as compared with the computational results in ethanol. Moreover, the optimization of **B** was performed at the same level of theory (Table 2). Generally, the results indicate that the optimization of **B** in ethanol offers more closer values than in the gas phase as compared to the X-ray crystallography data [19], Moreover, the values of some bonds were the same as the original ones extracted from the X-ray crystallography data for **B**, such as C3–C4, N6–C7, and N8–C12.

Hirshfeld surface analysis. A detailed analysis is made using Crystal Explorer 3.1 [15] to study various intermolecular interactions such as O···H, N···H, O···Cl, S···H, C···S, Cl···Cl, H···H, C···H, C···C and other types of close contacts existing in the crystal structures of **A** and **B**. By means of decomposed two-dimensional fingerprint maps [15], the intermolecular interactions involved in crystal packing can be quantified and visualized. Generally, the Hirshfeld surface was generated for a molecule in the crystal package plotted with various properties such as d_e (a distance to from the Hirshfeld

surface to the nearest atom outside the surface), d_i (a distance from the Hirshfeld surface to the nearest atom inside the surface), d_{norm} (a normalized contact distance), shape index and curvedness to demonstrate and investigate intermolecular interactions. White color in the Hirshfeld surface diagrams determines the contacts with distances equal to the sum of the van der Waals radii and red and blue colors represent the close contacts with distances shorter than and longer than the van der Waals radii, respectively. Using the Hirshfeld surface diagram, we recognized and represented the intermolecular interactions shown in Fig. 2. The intermolecular H···H contacts are predominant in **A** and **B** with the corresponding contributions of 31.5% and 32.3%, respectively.

The relative contributions of O···H/H···O contacts are 16.9% and 9.5% respectively as the second and fourth major contributions for **A** and **B**, respectively. Taking into account the intermolecular contributions of **A** and **B** atoms, the lowest amounts belong to Cl---Cl and C---O/O---C close contacts with 0.8% and 0.1% contributions for **A** and **B**, respectively.

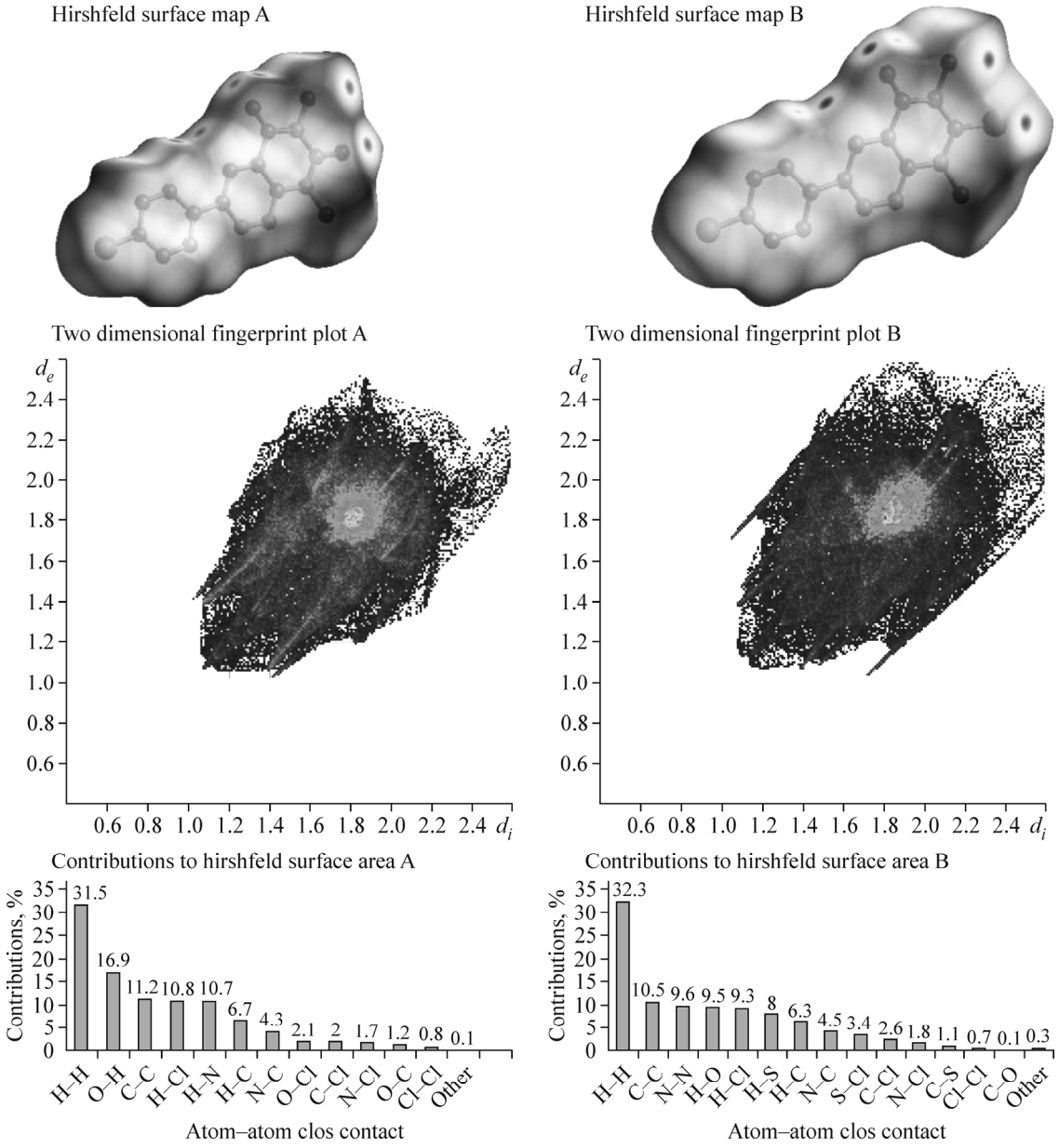

Fig. 2. Views of the Hirshfeld surfaces mapped with d_{norm}, fingerprint plots and the corresponding contributions to the Hirshfeld surface areas for different intermolecular close contacts for **A** and **B**.

Vibrational analysis. Experimental IR frequencies of 6,8-dimethyl-3-(4-chlorophenyl)-7-oxo-7,8-dihydropyrimido[4,5-*c*]pyridazin-5(6*H*) one (X = O) revealed the peaks corresponding to key functional groups for C–H aromatic (3056-3096 cm^{-1}), C–H aliphatic (2954 cm^{-1}), C=O (1672, 1720 cm^{-1}), C=C (1450 cm^{-1}), C=N (1597 cm^{-1}) and C–Cl (744 cm^{-1}), and in the case of 6,8-dimethyl-3-(4-chlorophenyl)-7-thioxo-7,8-dihydropyrimido[4,5-*c*]pyridazin-5(6*H*)-one (X = S), the peaks are revealed at 3055-3093 cm^{-1} (C–H aromatic), 2944 cm^{-1} (C–H aliphatic), 1689 cm^{-1} (C=O), 1430 cm^{-1} (C=C), 1595 cm^{-1} (C=N) and 740 cm^{-1} (C–Cl).

Furthermore, we calculated the vibrational frequencies of **A** and **B** by the B3LYP method. The C–H stretching frequencies of the **A** structure were observed at 3187 cm^{-1}, 3192 cm^{-1}, 3197 cm^{-1}, 3206 cm^{-1}, 3210 cm^{-1}, and 3216 cm^{-1}, while for **B** they were 3188 cm^{-1}, 3190 cm^{-1}, 3199 cm^{-1}, 3207 cm^{-1}, 3211 cm^{-1}, and 3218 cm^{-1}, in the gas phase, respectively. The peaks of **A** and **B** in the ranges 3056-3096 cm^{-1} and 3055-3093 cm^{-1} were assigned to the characteristic C–H aromatic stretching mode while the peaks at 2954 cm^{-1} and 2944 cm^{-1} were assigned to C–H aliphatic. The C=O stretching bands were observed at 1680 cm^{-1} and 1738 cm^{-1} for **A**, while in **B** this band was observed at 1713 cm^{-1}. A band at 784 cm^{-1} was assigned to the characteristic C–Cl stretching mode in the DFT calculation. The band assigned to C–C and N–N are conserved and appeared between 1591-1633 cm^{-1} and 1167-1194 cm^{-1} for **A** while they were at 1523-1631 cm^{-1} and 1176-1193 cm^{-1} for the same bands in **B** [30, 31].

Corresponding electronic properties. HOMO–LUMO and MEP plots of **A** and **B**. In order to understand the electronic properties of **A** and **B**, total densities of states (DOSs) of **A** and **B** were calculated (Fig. 3). The HOMO-LUMO energy gap (E_g) was calculated for **A** and **B** using the (B3LYP) hybrid correlation functional with the 6-311++G** basis set. The energies of the HOMO (E_H), mainly acting as an electron donor, and the LUMO (E_L), generally acting as an electron acceptor, are calculated and gathered in Table 3. The HOMO energies for **A** and **B** are –6.76 eV and –6.49 eV, while these values are –2.88 eV and –3.02 eV for LUMOs, with E_g of 3.88 eV and 3.47 eV, respectively. The Fermi level energies (E_F) are –4.82 eV and –4.76 eV for **A** and **B**, and the dipole moment (DM) analysis reveals that both **A** and **B** were not considered to be polar (having a weak polarity) with 0.89 and 0.49 D, respectively. For the better understanding of the electronic properties of **A** and **B**, we calculated HOMO-1, HOMO-2, and HOMO-3 (–7.17 eV, –7.72 eV, and –7.78 eV) and also LUMO-1, LUMO-2, and LUMO-3 (–2.08 eV, –1.05 eV, and –0.68 eV), respectively. The most noticeable change occurred in

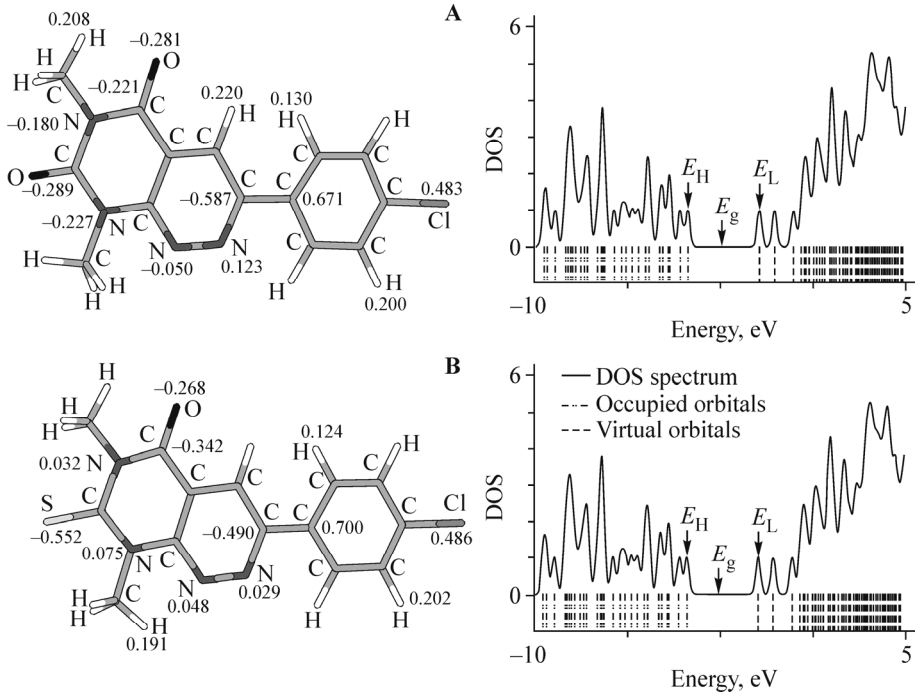

Fig. 3. Calculated natural charge of all atoms and DOS plots of **A** and **B** structures.

TABLE 3. Electronic, QMD, and Dipole Moment Values Extracted from the Calculation Results for **A** and **B**

Property	Gas		Solvent		Property	Gas		Solvent	
	A	**B**	**A**	**B**		**A**	**B**	**A**	**B**
HOMO, eV	–6.76	–6.49	–6.74	–6.52	μ, eV	–4.82	–4.76	–4.77	–4.72
LUMO, eV	–2.88	–3.02	–2.80	–2.92	η, eV	1.94	1.74	1.97	1.80
E_g, eV	3.88	3.47	3.94	3.60	ω, eV	5.99	6.52	5.77	6.19
E_F, eV	–4.82	–4.76	–4.77	–4.72	*S*, eV	0.26	0.29	0.25	0.28
DM, D	0.89	0.49	0.89	0.49					

the LUMO energy (about 1.4 eV), while the HOMO has just undergone a 1.11 eV change from the ground state. The natural bond orbital (NBO) analysis was performed for structures of **A** and **B**. The atomic charge distribution in the structures of **A** and **B** at the B3LYP/6-311++G** level of theory is shown in Fig. 3.

Furthermore, the molecular electrostatic potential (MEP) plot illustrates the electronegativity and electropositivity of a structure. As can be observed from these plots for **A** and **B**, the O1 and O2 atoms and the N1–N2 bond play the role of electronegative positions (represented via red color) while their most electropositive parts are in C17–H17A and C18–18A > C11–H11A, H11B, and H11C ~ C12–H12A, H12B, and H12C ~ C15–H15A, H15B, and H15C positions. The corresponding MEP plot of **B** also demonstrates high resemblance within the electronegativity and electropositivity of the atoms and their surrounding areas except for the O atoms of **A** and the S atom of **B.** The O atom due to a higher electronegativity than that of the S atom surely has more electronegative nature than the S atom, as is seen from the MEP plots (Fig. 4).

Quantum molecular descriptors for A and B. The quantum molecular descriptors (QMDs), such as hardness η, softness S, chemical potential μ, and electrophilicity index ω, can be calculated using HOMO, LUMO an E_g. The best definition of the global hardness is the resistance to deformation in the presence of an electric field whose field strength is directly proportional to the stability of the system. The resistance of a species against deformation in the presence of an electric field defined as the hardness of a species and the softness has an opposite relationship with its hardness. QMDs for **A** and **B** were calculated (Table 3); the hardness and softness values for **A** are 1.94 eV and 0.26 eV while they are 1.74 eV and 0.29 eV for **B**, respectively. These results are attributed to the effects of the O atom of **A** as compared to the S atom of **B**. **A** has a higher chemical potential (μ) than **B**, as a result of their X atom, they being 5.99 eV and 6.52 eV, respectively.

CONCLUSIONS

The computational optimization of the structural and electronic properties of **A** and **B** in the gas and solvent (ethanol) phases, which was performed using the B3LYP correlation functional with the 6-311++G** basis sets, revealed no meaningful distinctions between the experimental and theoretical data, confirming the better reliability of results of the

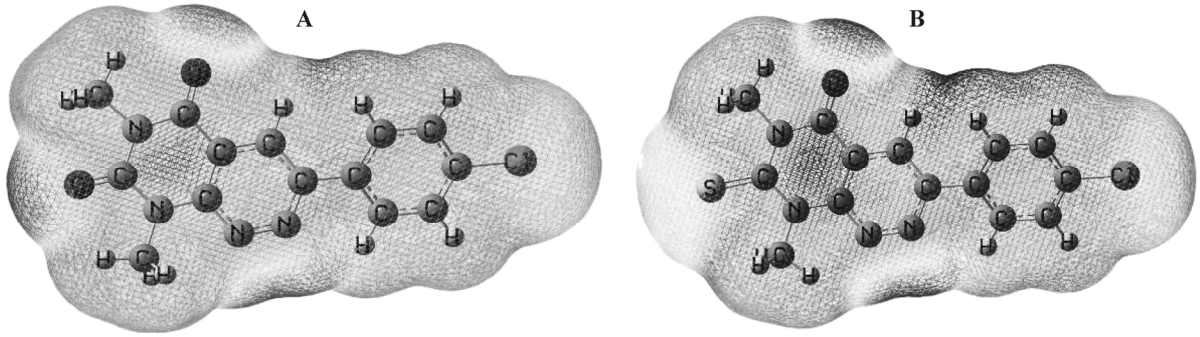

Fig. 4. MEP plots of the theoretically optimized compounds.

optimizations in the solvent (ethanol) phase. The Hirshfeld surface analysis along with the corresponding fingerprint plots stand for more contributions of H---H > O---H > C---C > H---Cl > H---N and H---H > C---C > N---N > H---O > C---Cl for the first five major contributions in **A** and **B**. The simulated IR spectra of **A** and **B** demonstrated good agreement with the experimental data.

We are grateful to the Urmia University for financial support. We also thank the Sayad Shirazi Hospital, Golestan University of Medical Sciences, Gorgan and Young Researchers and Elite Club of Gorgan Branch, Iran.

REFERENCES

1. S. C. Benson, C. A. Palabrica, and J. K. Snyder, *J. Org. Chem.*, **52**, 4610-4614 (1987).
2. F. Rohet, C. Rubat, P. Coudert, and J. Couquelet, *Bioorg. Med. Chem.*, **5**, 655-659 (1997).
3. J. A. Tucker, D. A. Allwine, K. C. Grega, M. R. Barbachyn, J. L. Klock, J. L. Adamski, S. J. Brickner, D. K. Hutchinson, C. W. Ford, G. E. Zurenko, R. A. Conradi, P. S. Burton, and R. M. Jensen, *J. Med. Chem.*, **41**, 3727-3735 (1998).
4. E. Sotelo and E. Ravina, *Synth. Commun.*, **32**, 1675-1680 (2002).
5. M. Gyoten, H. Nagaya, S. Fukuda, Y. Ashida, and Y. Kawano, *Chem. Pharm. Bull.*, **51**, 122-133 (2003).
6. A. Coelho, E. Sotelo, H. Novoa, O. M. Peeters, N. Blaton, and E. Ravina, *Tetrahedron*, **45**, 3459-3463 (2004).
7. N. Tamayo, L. Liao, M. Goldberg, D. Powers, Y.-Y. Tudor, V. Yu, L. M. Wong, B. Henkle, S. Middleton, R. Syed, T. Harvey, G. Jang, R. Hungate, and C. Dominguez, *Bioorg. Med. Chem. Lett.*, **15**, 2409-2413 (2005).
8. R. R. Nagawade, V. V. Khanna, S. S. Bhagwat, and D. B. Shinde, *Eur. J. Med. Chem.*, **40**, 1325-1330 (2005).
9. C. Altomare, S. Cellamare, L. Summo, M. Catto, and A. Carotti, *J. Med. Chem.*, **41**, 3812-3820 (1998).
10. G. A. Hamilton, in: *Progress in Bioorganic Chemistry*, E. T. Kaiser and F. J. Kezdy (eds.), Wiley, New York, **1**, 83 (1971).
11. D. J. Brown, in: *Comprehensive Heterocyclic Chemistry*, A. R. Katritzky and C. W. Rees (eds.), Pergamon, Oxford, **3**, 57-155 (1984).
12. H. Wamhoff, J. Dzenis, and K. Hirota, *Adv. Heterocycl. Chem.*, **55**, 129-259 (1992).
13. M. L. Roldán, A. E. Ledesma, A. B. Raschi, M. V. Castillo, E. Romano, and S. A. Brandán, *J. Mol. Struct.*, **1041**., 73-81 (2013).
14. L. T. Jr. Sein, *J. Mol. Struct.*, **1022**, 181-188 (2012).
15. B. Sjöberg, S. Foley, B. Cardey, and M. Enescu, *Spectrochim. Acta A*, **128**, 300-311 (2014).
16. J. M. Ramos, M. M. T. de Cruz, A. C. Jr. Costa, G. F. Ondar, G. B. Ferreira, L. Raniero, A. A. Martin, O. Versiane, and C. A. Téllez Soto, *Spectrochim. Acta A*, **97**, 1041-1051 (2012).
17. S. Sebastian, S. Sylvestre, N. Sundaraganesan, M. Amalanathan, S. Ayyapan, K. Oudayakumar, and B. Karthikeyan, *Spectrochim. Acta A*, **107**, 167-178 (2013).
18. Y. Zhang, X.-Y. Chen, H.-J. Wang, K.-S. Diao, and J.-M. Chen, *J. Mol. Struct. THEOCHEM*, **952**, 16-24 (2010).
19. J. Khalafy, M. Rimaz, H. Rabiei, and L. Panahi, *J. Sulfur. Chem.*, **34**, 395-406 (2013).
20. M. J. Frisch, G. W. Trucks, H. B. Schlegel, G. E. Scuseria, M. A. Robb, J. R. Cheeseman, V. G. Zakrzewski, J. A. Jr. Montgomery, R. E. Stratmann, J. C. Burant, S. Dapprich, J. M. Millam, A. D. Daniels, K. N. Kudin, M. C. Strain, O. Farkas, J. Tomasi, V. Barone, M. Cossi, R. Cammi, B. Mennucci, C. Pomelli, C. Adamo, S. Clifford, J. Ochterski, G. A. Petersson, P. Y. Ayala, Q. Cui, K. Morokuma, D. K. Malick, A. D. Rabuck, K. Raghavachari, J. B. Foresman, J. Cioslowski, J. V. Ortiz, A. G. Baboul, B. B. Stefanov, G. Liu, A. Liashenko, P. Piskorz, I. Komaromi, R. Gomperts, R. L. Martin, D. J. Fox, T. Keith, M. A. Al-Laham, C. Y. Peng, A. Nanayakkara, C. Gonzalez, M. Challacombe, P. M. W. Gill, B. Johnson, W. Chen, M. W. Wong, J. L. Andres, C. Gonzalez, M. Head-Gordon, E. S. Replogle, and J. A. Pople, *Gaussian 98*, P. Gaussian Inc., Pittsburgh, PA (1998).
21. C. Lee, W. Yang, and R. G. Parr, *Phys. Rev. B*, **37**, 785 (1988).

22. A. Soltani, F. Ghari, A. Dehno Khalaji, E. Tazikeh Lemeski, K. Fejfarova, M. Dusek, and M. Shikhi, *Spectrochim. Acta A*, **139**, 271-278 (2015).
23. A. Frisch, A. B. Nielson, and A. J. Holder, *GaussView Users Manual*, Gaussian Inc., Pittsburgh, PA (2000).
24. R. G. Parr and W. Yang, *Density Functional Theory of Atoms, Molecules*, Oxford University Press, Oxford, New York (1989).
25. R. G. Parr and R. G. Pearson, *J. Am. Chem. Soc.*, **105**, 7512-7516 (1983).
26. A. Soltani, M. T. Baei, E. Tazikeh Lemeski, S. Kaveh, and H. Balakheyli, *J. Phys. Chem. Solids.*, **86**, 57-64 (2015).
27. A. Soltani and M. Bezi Javan, *RSC Adv.*, **5**, 90621-90631 (2015).
28. T. Koopmans, *Physica.*, **1**, 104-113 (1933).
29. R. G. Parr, L. Szentply, and S. Liu, *J. Am. Chem. Soc.*, **121**, 1922-1924 (1999).
30. V. Ferraresi-Curotto, G. A. Echeverria, O. E. Piro, R. Pis-Diez, and C. Gonzalez-Baro, *Spectrochim. Acta A*, **137**, 692-700 (2015).
31. A. Esme and S. Gunesdogdu Sagdinc, *J. Mol. Struct.*, **1048**, 185-195 (2013).